ROYAL AERONAUTICAL SOCIETY

REGULAR PAPER

Numerical modelling of Lamb wave propagation in 2D plate structures

L. Pollock [ID] and G. Wild [ID]

School of Engineering and Information Technology, UNSW Canberra, ACT, 2612 Australia
Corresponding author: L. Pollock; Email: L.Pollock@adfa.edu.au

Abstract
Lamb waves are a growing method for the Non-Destructive Testing and Evaluation (NDT&E) and structural health monitoring (SHM) of aerospace vehicles. These guided waves can propagate over large distances and have a strong tendency to interact with damage. Whilst several methods exist for the modelling of Lamb wave propagation, this paper is the first to introduce a first principles numerical model that can efficiently and accurately predict the behaviour of Lamb waves. The numerical model is easier to understand and implement compared with analytical solutions and significantly faster than discretised numerical methods. The numerical model is presented in detail for an isotropic and homogenous plate, along with validation against the industry accepted, WaveForm Revealer 3 (WFR3) software. The results show a mean correlation across all assessed parameters of 90.4% and 96.6% for the symmetric and antisymmetric modes, respectively. Further discussion is provided on future developments to the model, including on the topic of high temperature effects, anisotropic materials and edge reflections.

Nomenclature

μ, λ	Lamé's parameters
ν	Poisson's ratio
ρ	Density
u	Longitudinal displacement
v	Transverse displacement
A, B, C, D	Arbitrary constants
p, q	Dispersive wavenumbers
k	Wavenumber
ω	Circular frequency
f	Linear frequency
c_L	Longitudinal wave velocity of the bulk material
c_T	Transverse wave velocity of the bulk material
E	Young's modulus
c_g	Group velocity
c_p	Phase velocity
ϕ	Phase
T	Temperature
α	Coefficient of thermal expansion
Q_{ij}	Stiffness coefficients along the ply axis
A_{ij}^*	In plane stiffness terms

1.0 Introduction

Non-destructive testing (NDT) has been around for over 100 years, with one of the very first applications being in the railroad industry [1]. The 1970s significantly changed the field of NDT with the emergence of the discipline of fracture mechanics [1]. This enabled the prediction of whether a crack of a given size would fail under a given load if the relevant material property or fracture toughness was known. Laws to predict the rate of growth of cracks under cyclic loading were also developed. With these laws, it became possible to use structures with known defects, if the sizes of the defects were known [2]. That is, design incorporated a new approach, and they became "damage tolerant designs" [3]. Components with known defects could be used as long as the defects did not grow past a critical limit, which could result in a catastrophic failure. This presented a new challenge for NDT, 'simple' detection of flaws was no longer enough, quantitative information was needed about the size of flaws to enable predictions of the component's residual life. That is, non-destructive evaluation (NDE) [1, 4].

Structural Health Monitoring (SHM) is an emerging area which brings together NDE with smart technologies and materials [5]. The drive for SHM in the aerospace industry lies with the need to improve safety, for both aerospace manufacturers and operators. Maintenance activities can account for as much as 20% of the direct operating costs, and human error in maintenance contributes to 15% of all aircraft accidents [5]. Beyond that, reliable SHM would allow for less conservative design philosophies to be used, leading to significant weight savings on future aircraft whilst improving the safety of passengers. The rapid advances that have been made in recent decades in sensor technology, smart materials and innovative structural concepts are leading to the practical use of SHM. One such area is the use of ultrasonic guided waves [6, 7], a direct evolution of traditional ultrasonic NDT.

Simulation of ultrasonic guided wave-based NDT and NDE for SHM is onerous [6]. While the use of finite element analysis (FEA) has become more common [8], there are limitations and issues with such a method. Specifically, FEA can be computationally intensive [9]. Reducing computational effort is essential for airframe digital twins [10, 11], especially if an intelligent digital twin is used onboard, in flight [12]. In this work, a simple numerical model for guided wave propagation in 2D plate structures is presented. These structures made specifically of aluminium alloys are representative of those used to skin aircraft [13, 14].

2.0 The numerical model

The original analysis of guided waves in thin plates was published by Lamb in 1917 [15] and derives itself from an interrogation of the elastodynamic Navier-Cauchy equations for isotropic materials [16].

$$\mu v_{i,jj} + (\lambda + \mu)v_{j,ji} + \rho f_i = \rho \ddot{v}_l \tag{1}$$

The geometry is simple, the thin plate is a solid medium which is bounded on the top and bottom by parallel planes which are a distance $2h$ apart, as depicted in Fig. 1 [17]. In the horizontal distance within the plate, the dimensions are unbounded, and it is also assumed that there is no medium outside the upper and lower bounds of the solid plate. In a bulk solid medium, mechanical waves can propagate as longitudinal (pressure) waves, or as lateral (shear) waves. In a plate, the close nature of bounding planes results in a mixing of these types of waves, and interestingly results in the production of two unique propagation modes. These are the symmetric wave which is an even function of the displacement of the medium in z, where $u(z) = u(-z)$, and the antisymmetric wave, which is an odd function of the displacement of the medium in z, where $-u(z) = u(-z)^{(17)}$. The longitudinal component of the displacement u and a transverse component w have the form,

$$u = i(kA \cos(pz) + qB \cos(qz))e^{ik(x-ct)} \tag{1.1}$$

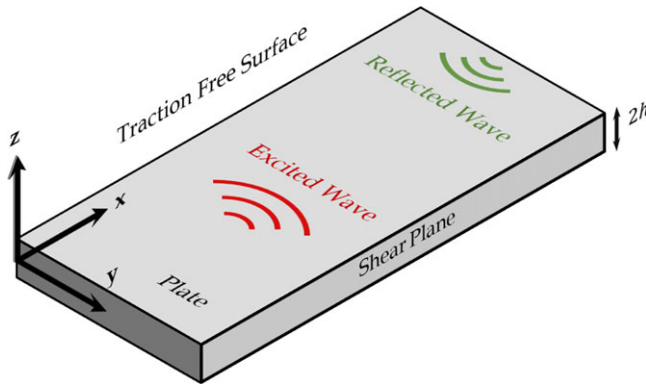$$w = (-pA \sin(pz) - kB \sin(qz))e^{ik(x-ct)} \tag{1.2}$$

Figure 1. *The general setup and co-ordinate system for a guided Lamb wave.*

for symmetric modes, and

$$u = i(kC \sin(pz) - qD \sin(qz))e^{ik(x-ct)} \tag{2.1}$$

$$w = (pC \cos(pz) - kD \cos(qz))e^{ik(x-ct)} \tag{2.2}$$

for antisymmetric modes. While A, B, C and D are arbitrary constants, the coefficients p and q represent the dispersive wavenumbers, and are given by,

$$p^2 = \frac{\omega^2}{c_L^2} - k^2 \tag{3.1}$$

$$q^2 = \frac{\omega^2}{c_T^2} - k^2 \tag{3.2}$$

where ω is the circular frequency of the wave, k is the wavenumber determined by the phase velocity of the wave at ω, c_L is the longitudinal wave velocity of the bulk material and c_T is the transverse wave velocity of the bulk material.

$$c_L = \sqrt{\frac{\lambda + 2\mu}{\rho}} \tag{4.1}$$

$$c_T = \sqrt{\frac{\mu}{\rho}} \tag{4.2}$$

The variables λ and μ represent the Lamé constants as given below [18].

$$\lambda = \frac{E\nu}{(1+\nu)(1-2\nu)} \tag{5.1}$$

$$\mu = \frac{E}{2(1+\nu)} \tag{5.2}$$

The boundary conditions are that $t_{xz} = s_{zz} = 0$ on $z = \pm h$ [19]. The result of imposing these boundary conditions is that Equations (1.1) to (2.2) only have nontrivial solutions if,

$$\frac{\tan(qh)}{\tan(ph)} = -\frac{4k^2 pq}{(q^2 - k^2)^2} \tag{6.1}$$

$$\frac{\tan{(ph)}}{\tan{(qh)}} = -\frac{4k^2pq}{(q^2 - k^2)^2} \tag{6.2}$$

for the symmetric and antisymmetric modes, respectively [19].

The important result is that Lamb waves are dispersive, given the velocity depends on the product of h and ω, or the frequency-thickness product. That is, any arbitrary wave, which based on Fourier's theorem can be described as the sum of many sinusoidal waves, will experience dispersion, as well as generating two wave modes that travel independently of each other. The group velocity given as $c_g = \frac{d\omega}{dk}$ can be related to the phase velocity through Equation (7).

$$c_g = c_p^2 \left[c_p - (fh)\frac{dc_p}{d(fh)} \right]^{-1} \tag{7}$$

Where *fh* represents the frequency-thickness product of the case. The frequency-thickness product is often used as the independent variable as it allows for calculation of the phase velocity independent of the thickness of the plate. Modelling the propagation of an ultrasonic guided wave in a plate structure can be achieved using the previously stated fact. Any signal is a sum of sinusoidal waves. Each sinusoidal wave will have a velocity dictated by the dispersive relationship, which is a function of the material properties and the plate thickness. Consider a typical Gaussian apodised sinusoidal signal,

$$f(t) = (A\cos{(\omega t)})e^{t^2/2c^2} \tag{8}$$

The Fourier transform of this signal will be a Gaussian distribution of frequencies about the central frequency, ω [20]. Rather than defining analytically what the Fourier transform of (8) is, a discrete numerical approximation of the function can be defined with a set sampling rate. The fast Fourier transform (FFT) of this discrete signal will then provide the phase and amplitude information for all the sinusoids that sum together to form this signal. In the frequency domain, the spacing of these constituent signals (df) is derived from the sampling rate ($1/dt$) and the total number of samples (n), such that,

$$\Delta f = \frac{1}{n\Delta t} \tag{9}$$

Knowing each frequency, the dispersion for each can be determined. There are two options, root finding algorithms can be used for Equations (6.1) and (6.2) to determine the valid wave speed at each frequency, or a lookup table for the given material with a given thickness can be utilised. The second provides a more computationally efficient means of determining the dispersion but is less general purpose. For each signal, a time component can be determine based on the distance between the transmitter and receiver, and the wave speed at that frequency. Importantly, the relative phase information from the FFT is preserved and used as the initial phase offset of the sinusoid before adding the traveling wave component.

For the received signal, there is no inverse problem that needs to be solved. That is, each of the signals at the receiver location do not have their amplitude and phase information taken to for the FFT of the received signal, which is the inverted (iFFT) to give the received time domain signal. Rather, the direct sum of the array of sinusoids is the time domain signal. Effectively, the computationally intensive solution to the inverse problem is solved with the novel application of first principles physics. The overall procedure is illustrated in Fig. 2.

3.0 Other modelling approaches

Several numerical methods already exist for the modelling of Lamb waves in plate-like materials such as the finite element method (FEM), spectral element method (SEM), and semi-analytical finite element method (SAFE). These numerical modelling techniques are often time intensive in both setup and
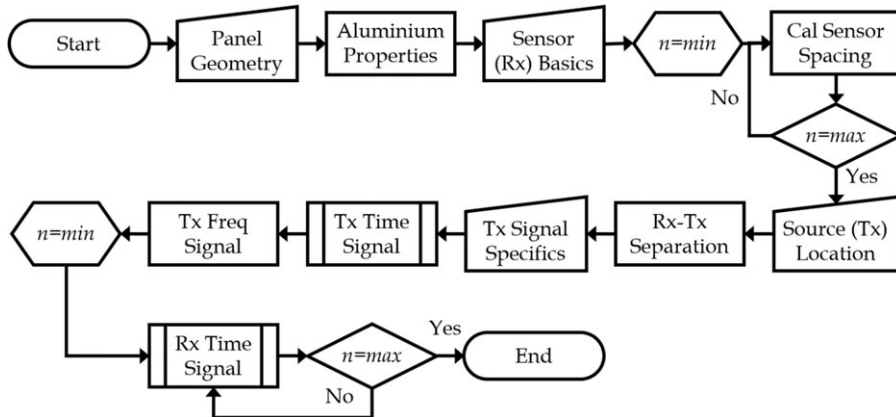
Figure 2. *The process for the numerical model shown as a flow chart.*

operation, requiring extensive resources. However, the use of such methods permits analysis of complex structures such as composite materials, stepped geometries, assemblies and damage interaction.

3.1 Finite element analysis (FEA)

The finite element approach for the computation of Lamb wave behaviour is the most versatile and resource intensive. Using FEA, the entire structural model is spatially discretised, and a series of partial differential equations are solved using adequate boundary conditions for the time response of the model. FEA is a powerful tool for the exploration of Lamb wave responses to various geometries [21], materials [22], damages [23–25] and sensor-material interactions [26]. Analysis of Lamb waves using FEA is also one of the most accessible methods due to the availability of commercial software. However, the high resource demand has led to the development of various other numerical methods.

3.2 Spectral element analysis (SEA)

An alternative method to FEA is that of SEA developed principally for work with fluid flows [27]. SEA has a high degree of similarity to FEA, but offers large computational savings due to the use of Lagrange interpolation functions [28]. The SEA method has been used in similar applications to FEA such as material modelling [22], damage [29] and sensor-material interactions [30]. Ultimately, SEA offers significant benefits over FEA but is otherwise less accessible due to the lack of commercial software available.

3.3 Semi-analytical finite element analysis (SAFE)

The semi-analytical method for the simulation of Lamb wave propagation in elastic wave guides has been studied intensively. The SAFE method offers computational savings over other, pure, finite element methods [31]. The SAFE method was first formulated by Aalami [32] in 1973. Using SAFE, the waveguide is discretised across the cross-section whilst an exponential function is used in the propagation direction [31]. The SAFE method has been used for the efficient calculation of the dispersive properties of a Lamb wave in anisotropic laminates and has been shown to have exact solutions for homogenous materials [33]. The SAFE method is an effective tool for calculating the propagation of Lamb waves in irregular and non-planar geometries [34–36]. Recent work with SAFE has involved the modelling of more complex materials and interactions such as viscoelastic effects in composite mediums [37],

boundary reflection interactions [32], reflection and transmission behaviour for damage and discontinuities [38], pre-stressed materials [39] and leaky Lamb wave behaviour [40]. The SAFE method requires integration of analytical equations with typically finite element methods and is generally developed for individual cases.

3.4 WaveForm Revealer 3

As an alternative, WaveForm Revealer 3 (WFR3) developed by the University of South Carolina is an analytical method for the modelling of Lamb wave propagation by the convolution of a user input function with a structural transfer function in the frequency domain [41]. The structural transfer function is derived by Giurgiutiu [18, 41] and given below.

$$G(u, \omega) = S(\omega)e^{ik^S u} + A(\omega)e^{ik^A u} \tag{10}$$

Where the superscript S and A and functions $S(\omega)$ and $A(\omega)$ correspond to the symmetric and anti-symmetric components, respectively. These are given below.

$$S(\omega) = -\frac{i\frac{a\tau_0}{\mu}\sin(k^S a)N_S(k^S)}{D'_S(k^S)} \tag{11.1}$$

$$A(\omega) = -\frac{i\frac{a\tau_0}{\mu}\sin(k^A a)N_A(k^A)}{D'_A(k^A)} \tag{11.2}$$

The analytical model for WFR3 is programmed in MATLAB and operated through a graphical user interface (GUI). WFR3 is also capable of modelling Lamb wave damage interactions such as transmission, reflection and conversion behaviour. WFR3 has been validated against FEM and experimental testing such that it is now favoured by industry and academia [41]. Moreover, the analytical method offered significant computational time savings over typical numerical techniques. As a result of the low-resource requirement of WFR3, it has been used in later sections to verify the proposed first principles numerical model.

4.0 Validation

The first step in deploying the numerical model is to determine the dispersion relationships for the given material. Firstly, a range of phase velocities must be selected in which the solution to the Rayleigh-Lamb equation is predicted to exist. These selected phase velocities are used to calculate the predicted wave numbers for the inputted frequency range, which are then used to determine the p and q constants as given in Equations (3.1) and (3.2). To begin solving the Rayleigh-Lamb equation, it is better to rearrange it into a more useful form suitable for solving with a numerical method. The rearranged forms of Equations (6.1) and (6.2) are given below in subscript notation.

$$\frac{\tan(q_n h)}{\tan(p_n h)} + \frac{4k_n^2 q_n h}{(k_n^2 - q_n^2)^2} = f_n^S \tag{12.1}$$

$$\frac{\tan(q_n h)}{\tan(p_n h)} + \frac{(k_n^2 - q_n^2)^2}{4k_n^2 q_n h} = f_n^A \tag{12.2}$$

The exact solution for the wavenumber and hence, phase velocity occurs when $f_n = 0$, representing a root of the rearranged Rayleigh-Lamb equation. A variety of numerical solvers can be applied at this point such as the bisection, secant or Newton-Raphson method. For most solvers, an interval must be determined in which the root is known to lay. Hence, the range [n, n+1] in which a root is found is determined for the case that $f_{n+1} \cdot f_n < 0$. Discovery of this range restricts the search field, rendering the ability to apply the desirable solver. For the case of higher order wave modes, it must be acknowledged that more than one root may exist within the search field, requiring more rigorous methods. The search
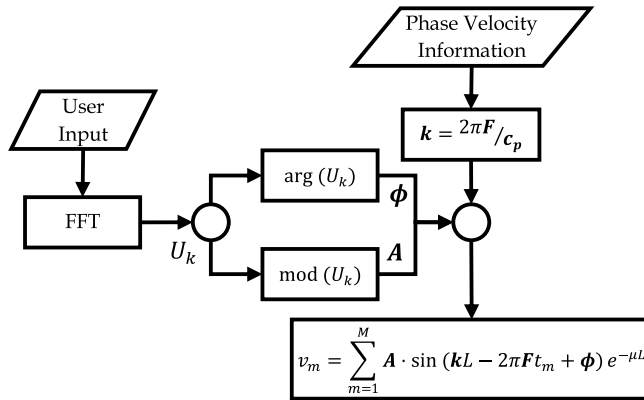
Figure 3. *Flow chart depicting the first principles numerical method.*
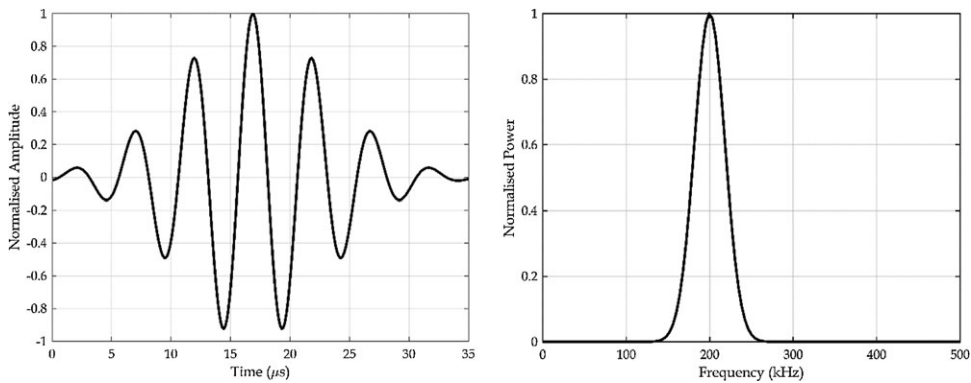

Figure 4. *The time domain input signal (left) and its frequency spectrum (right).*

resolution for the root can be coarse as the Rayleigh-Lamb equation has high smoothness and hence, a cubic spline may be fitted to the roots to improve the efficiency of the process. Once the phase velocities have been found for the given frequency range, the group velocities may be determined by applying a suitable finite difference approximation to Equation (7).

Following determination of the dispersive relationship, the numerical model may be applied as shown in Figs. 2 and 3. To validate the proposed method and evaluate it against common practices, a parametric study was performed for a range of variables. The numerical model was compared with the industry accepted and peer-reviewed software WFR3, developed by the University of South Carolina. The study was conducted using a Gaussian windowed sinusoid centred at a peak frequency of 200 kHz with a fractional bandwidth of 30% as the input signal, shown in Fig. 4. A Gaussian windowed function is used to reduce signal ringing effects [42, 43].

In performing the parametric study, the symmetric and antisymmetric wave modes were compared separately. The choice of sensor has a dramatic impact upon the amplitude ratio between the two modes, most notably; fibre Bragg gratings are much more sensitive to the symmetric mode as they measure in-plane displacement whilst piezoelectric transducers are generally more sensitive to the antisymmetric mode due to their measurement of out-of-plane displacement [44]. Hence, the amplitude relationship between the two modes would greatly differ dependent upon the sensor choice. Moreover, it has been shown that piezoelectric transducers can be carefully selected such that they may be tuned for the detection of selected wave modes [45]. Ultimately, separation of the two modes allows for normalisation and for a sensor agnostic comparison. The relationship between the two wave modes is commutative and hence, separation will not affect the results.
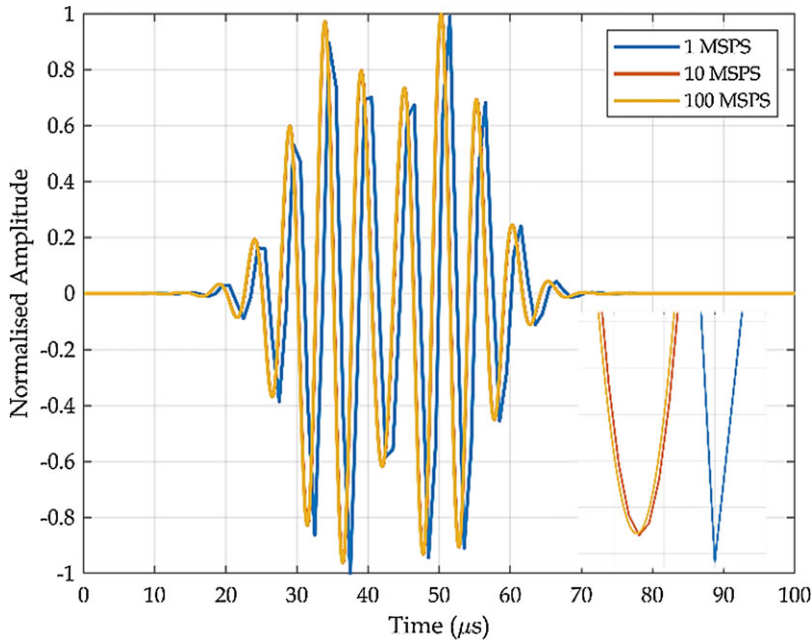
Figure 5. *A comparison of the propagated wave using the numerical model with different sampling frequencies.*

Data from the WFR3 software is exported with a sampling rate of 10 mega samples per second (MSPS). Hence, as a matter of consistency, the sampling frequency of the proposed model has been set to match this. Whilst the sampling frequency from the WFR3 software does not affect the overall results, the sampling frequency in the numerical model is used for the constitutive frequency selection. As such, varying the sampling frequency of the numerical model could have a minor effect on the results of the study. Nonetheless, as the sampling frequency is increased, it produces results that are more like the analytical solution. At a sampling frequency of 10 MSPS, it is expected that the numerical model results should offer a high degree of similarity to the analytical solution. A comparison of three sampling frequencies is shown below for the numerical model output in Fig. 5.

At a value of 1 MSPS it is evident that the wave packet is not smooth. At both sampling frequencies of 10 MSPS and 100 MSPS, the results are near identical, and the wave packets can hardly be distinguished from one another. The effect of frequency selection between 1 MSPS and 10/100 MSPS is evident as there is a phase delay between the signals. Ultimately, a sampling frequency between 10 MSPS and 100 MSPS should provide signal outputs that are akin to the analytical solution and any aliasing effects are negligible.

To evaluate the similarity between WFR3 and the numerical model, two methods have been employed. Firstly, the cross-correlation function has been used in the time domain. The cross-correlation function is a method of determining the lag between the location of highest correlation of two signals. A small lag indicates that the signals are very close to their highest point of correlation. If the lag value across all the parametric trials is relatively constant, this is a possible indicator that there is a constant phase delay between the two methods but that they otherwise produce very similar results. The cross-correlation is a useful tool in determining this phase delay but is not a definite method for determining similarity. The method for calculating cross-correlation is given below for two, time dependent signals $x_1(t)$ and $x_2(t)$ where signal two is a copy of signal one separated by a time delay (lag) τ_{12} and attenuation A. Both signals are assumed to have independent, Gaussian noise components given by $n_1(t)$ and $n_2(t)$.

For the parametric study both signals have no noise and hence, $n_1(t) = n_2(t) = 0$.

$$x_1 = s_1(t) + n_1(t) \tag{13.1}$$

$$x_2 = As_1(t + \tau_{12}) + n_2(t) \tag{13.2}$$

A perfect cross-correlation between two signals can only be obtained over an infinite period and hence, any calculation possesses a degree of truncation. The method for determining the cross-correlation function for a pair of discrete signals is given below where $\bar{x}_n$ is the complex conjugate of x_n.

$$\psi_j = \lim_{N \to \infty} \sum_{k=-N}^{N} x_{1_{k+j}} \cdot \bar{x}_{2_k} \tag{14}$$

The cross-correlation can be more efficiently calculated in the frequency domain where the lag can be determined as follows where $X_1(f)$ is the Fourier transform of signal one and $\bar{X}_2(f)$ is the complex conjugate of the Fourier transform of signal two.

$$\tau_{12} = \max \text{iFFT} \left(X_1(f) \cdot \bar{X}_2(f) \right) \tag{15}$$

The second measure of similarity used is Pearson's linear correlation. The correlation coefficient is a useful metric in determining a linear relationship between sets of data. As the time information, given as the independent variable, will be constant between data sets, the correlation coefficient may be used to compare the amplitude response of the two signals. However, if the signals are not properly aligned due to a possible phase delay, this metric would not prove useful. Hence, the cross-correlation is initially performed and then used to align the signals to the point of their maximum correlation before the correlation coefficient is calculated to determine the magnitude of correlation at this location. In this way, the combination of the two metrics should act as a robust way for determining similarity in both amplitude and phase. The Pearson's correlation coefficient is given below for two signals x_1 and x_2 with means of $\overline{x_1}$ and $\overline{x_2}$.

$$r = \frac{\sum_{i=1}^{N} \left(x_{1i} - \overline{x_1} \right) \left(x_{2i} - \overline{x_2} \right)}{\sqrt{\sum_{i=1}^{N} \left(x_{1i} - \overline{x_1} \right)^2 \sum_{i=1}^{N} \left(x_{2i} - \overline{x_2} \right)^2}} \tag{16}$$

A comparison of the dispersive relationships calculated from the numerical model and obtained from WFR3 are shown in Fig. 6. The resultant curves are for aluminium alloy 2024-T3.

The Pearson's linear correlation coefficient has been used to compare the two dispersion relationships. As can be seen, both wave modes are perfectly correlated with a correlation value of one. Hence, the dispersion information from both the proposed technique in the numerical model as well as the WFR3 software can be considered identical.

The remainder of the numerical model is validated against WFR3 over a range of material properties and variables as noted in Table 1. These variables are swept from the lower limit to the upper limit with the spacing specified. These properties are assessed over a range that is suitable for most materials. Symmetric and antisymmetric modes are compared independently as previously discussed.

The results of the parametric study are shown below in Fig. 7 with phase error, depicted as a time delay on the left and amplitude error, depicted as the Pearson's correlation coefficient shown on the right. Both sets of data show that the numerical model is comparatively very similar to the results obtained from WFR3. There are notably few outliers. WFR3 struggles to provide a solution as material properties approach non-physical values. Most notably, a Poisson's ratio of 0.05 produced a bad result. However, the numerical model continues to perform well in this regime and yields qualitatively accurate results. Nonetheless, the results indicate that the numerical model is capable of accurately calculating the propagation of Lamb waves.

The following sections detail several proposed improvements to the basic version of the numerical model, including how higher levels of fidelity may be incorporated.

Table 1. *The range of variables assessed in the numerical model validation*

	Lower limit	Spacing	Upper limit
Young's modulus (E)	50 GPa	25 GPa	300 GPa
Density (ρ)	500 kg/m^3	500 kg/m^3	5,000 kg/m^3
Plate thickness (h)	1 mm	1 mm	8 mm
Poisson's ratio (ν)	0.05	0.05	0.45
Distance (D)	50 mm	50 mm	500 mm
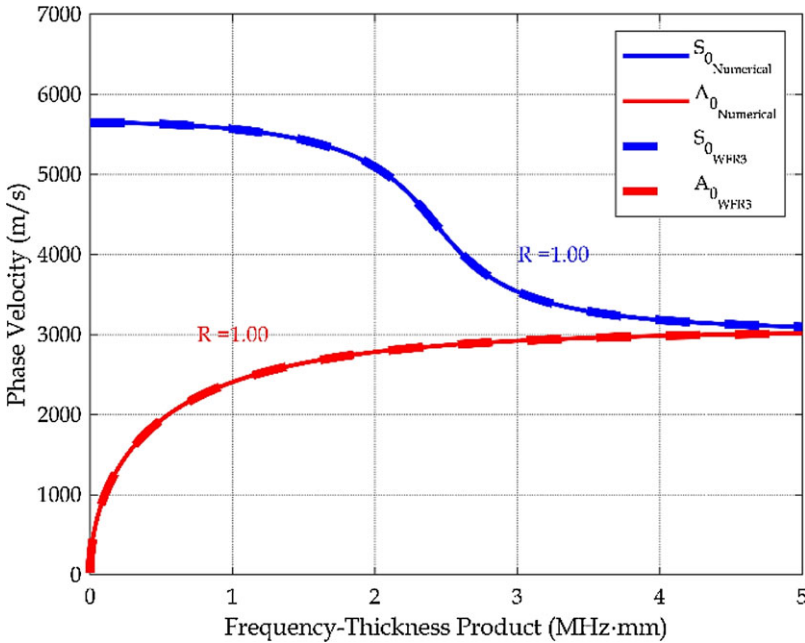
Figure 6. *A comparison of dispersion properties of aluminium from the numerical model and WFR3.*
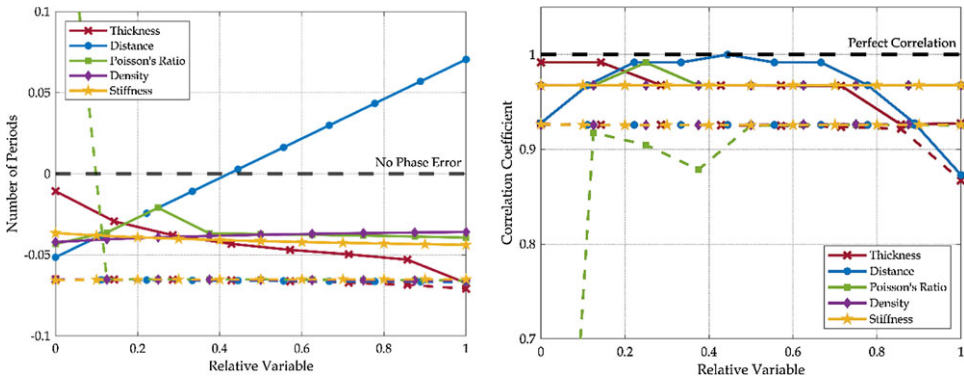
Figure 7. *Time delay comparison between the numerical model and WFR3 (left) and the Pearson's correlation coefficient of the signals (right). Antisymmetric modes are shown as solid lines and symmetric as dashed lines.*

5.0 Modelling extensions

5.1 High temperature effects

Whilst numerous advancements have been made in the fields of NDE and SHM, there remains several challenges, including operation in extreme environments. High-temperature sensors that can withstand such conditions are difficult and expensive to produce. Modelling of high-temperature Lamb waves allows for the optimisation of sensing systems to overcome some of these challenges. Aerospace fields that would see the biggest improvement from research in this area includes the health monitoring of propulsive systems and hypersonic vehicles.

Propulsion systems have recently been shown as the most common cause of fatigue failure in aircraft [46]. Moreover, whilst hypersonic flight has seen deployment of experimental vehicles (~TRL 5), mass production has been delayed, partly owing to the low reliability of some systems [47]. The extreme environments in which these vehicles operate introduce large uncertainties and sensitivities of which the use of SHM can aid in overcoming.

Whilst a suitable body of literature exists that explores the thermal effects on Lamb wave propagation, little work has been completed at temperatures of interest (> 1,000°C). Within this higher temperature range, it is expected that additional phenomena may be encountered that have not been considered in previous work. Materials for use in this temperature range including nickel-based superalloys, titanium aluminides and Ceramic Matrix Composites (CMCs) exhibit phenomena such as viscoelastic behaviour and creep that has not been characterised or modelled [48]. Moreover, accumulation of creep damage results in higher void content and cracking that can further influence acoustic behaviour and further engenders reflection-transmission and mode conversion [48].

First attempts can be made to model high-temperature Lamb waves by solving a temperature dependent Rayleigh-Lamb equation. Here, λ_T and μ_T are the first and second temperature dependent Lamé's constants, respectively. The temperature change ΔT is taken as the difference between the current temperature T and that of a reference temperature T_0. The half-thickness of the plate h with respect to the thickness at the reference temperature h_0 is then determined by considering the linear coefficient of thermal expansion α.

$$h(\Delta T) = h_0(1 + \alpha \Delta T) \tag{17}$$

Likewise, the density of the material with respect to the density at the reference temperature can be determined.

$$\rho(\Delta T) = \frac{\rho_0}{(1 + \alpha \Delta T)^3} \tag{18}$$

The variation in Young's modulus and Poisson's ratio were empirically derived by Augereau et al. [49] for aluminium 6061-T6 over a temperature range of 20°C to 220°C as given below. Material properties at high temperatures is arguably one of the biggest limitations in this area.
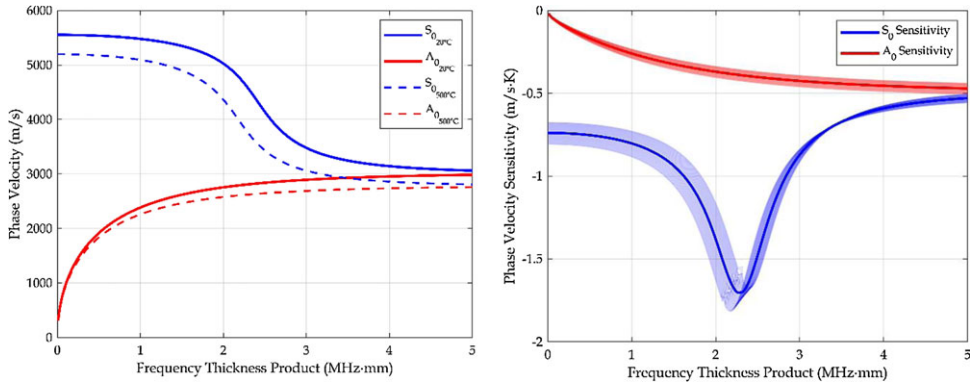
$$E = 77.59 - \frac{27.03 \cdot T}{10^3} - \frac{13.78 \cdot T^2}{10^6} \tag{19.1}$$

$$\nu = 0.317 + \frac{54.79 \cdot T}{10^6} + \frac{6.5 \cdot T^2}{10^9} \tag{19.2}$$

Taking the derivative of p and q with respect to temperature provides the following relationships.

$$p\frac{\partial p}{\partial T} = k\frac{\partial k}{\partial T} - k_L\frac{\partial k_L}{\partial T} \tag{20.1}$$

$$q\frac{\partial q}{\partial T} = k\frac{\partial k}{\partial T} - k_T\frac{\partial k_T}{\partial T} \tag{20.2}$$

Figure 8. *A comparison of dispersive phase velocities for aluminium (left) and the corresponding sensitivity (right). The solid and dashed lines correspond to the room temperature and 500°C solutions, respectively.*
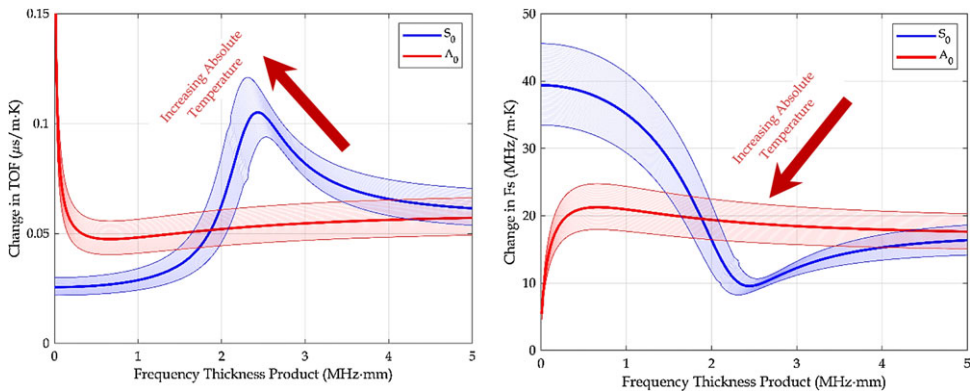
Figure 9. *Change in the signal time-of-flight (TOF) (left) and corresponding increase in sampling frequency (right).*

Where k_L and k_T are the longitudinal and transverse wave numbers, respectively. Finally, the group velocity C_G may be calculated as follows from the phase velocity C_P.

$$\frac{\partial C_G}{\partial T} = \frac{\partial C_P}{\partial T}\left(1 - \frac{k}{C_P}\frac{\partial C_P}{\partial k}\right) + k\left(\frac{\partial^2 C_P}{\partial k \partial T}\right) \tag{21}$$

A plot of the dispersive phase velocities for aluminium 6061-T6 as well as the corresponding temperature sensitivities are shown in Fig. 8. It is clear that an increase in temperature results in a decrease in the phase velocity of both wave modes but is more pronounced for the symmetric mode.

The change in the time-of-flight (TOF) of an acoustic signal as well as the corresponding increase in frequency is shown in Fig. 9. An example of a 200 kHz wave in a 3 mm plate that is transmitted over 250 mm with an increase from the reference temperature of 20°C would result in a change in the TOF of the symmetric mode by 0.134 μs and the antisymmetric mode by 0.239 μs.

5.2 Anisotropic materials

A further extension of the numerical model may include consideration of anisotropic materials. Such materials are commonplace in aerospace settings, primarily in the form of fibre reinforced polymers

(FRPs) and cold-rolled aluminium [50]. Adjustments can be made to the original model by including these effects in the form of directionally dependent material properties. The model can easily incorporate this modification by calculating the dispersion relationships for each direction of interest. Whilst such a method would account for the variation in wave speed, it would not capture the complex Lamb wave and shear horizontal wave coupling effects [51].

To model the anisotropic material properties in FRPs, classical laminate theory (CLT) is used to determine the directionally dependent material properties. We begin with the reduced stiffness coefficients of the material along the ply axis, knowing that $\frac{v_{12}}{E_1} = \frac{v_{21}}{E_2}$ [52].

$$Q_{11}(0) = \frac{E_1}{1 - v_{12}v_{21}} \tag{22.1}$$

$$Q_{22}(0) = \frac{E_2}{1 - v_{12}v_{21}} \tag{22.2}$$

$$Q_{12}(0) = \frac{v_{21}E_1}{1 - v_{12}v_{21}} \tag{22.3}$$

$$Q_{66}(0) = G_{12} \tag{22.4}$$

These coefficients must then be transformed along the laminate axis, where $c = \cos(\theta)$, $s = \sin(\theta)$.

$$\boldsymbol{Q}(\theta) = \boldsymbol{TQ}(0), \tag{23}$$

$$\boldsymbol{T} = \begin{bmatrix} c^4 & 2c^2s^2 & s^4 & 4c^2s^2 \\ c^2s^2 & c^4 + s^4 & c^2s^2 & -4c^2s^2 \\ s^4 & 2c^2s^2 & c^4 & 4c^2s^2 \\ c^3s & -cs\left(c^2 - s^2\right) & -cs^3 & -2cs\left(c^2 - s^2\right) \\ cs^3 & cs\left(c^2 - s^2\right) & -c^3s & 2cs\left(c^2 - s^2\right) \\ c^2s^2 & -2c^2s^2 & c^2s^2 & \left(c^2 - s^2\right)^2 \end{bmatrix}, \quad \boldsymbol{Q}(0) = \begin{matrix} Q_{11}(0) \\ Q_{12}(0) \\ Q_{22}(0) \\ Q_{66}(0) \end{matrix} \tag{24}$$

Next, we calculate the in-plane stiffness matrix terms for the stress resultants.

$$A_{ij}^* = \frac{1}{t} \sum_{k=1}^{n} Q_{ij}(\theta_k)(h_k - h_{k-1}) \tag{25}$$

Finally, the stiffness properties of the material along the laminate axis may be obtained.

$$E_x = A_{xx}^* - \frac{A_{xy}^{*2}}{A_{yy}^*} \tag{26.1}$$

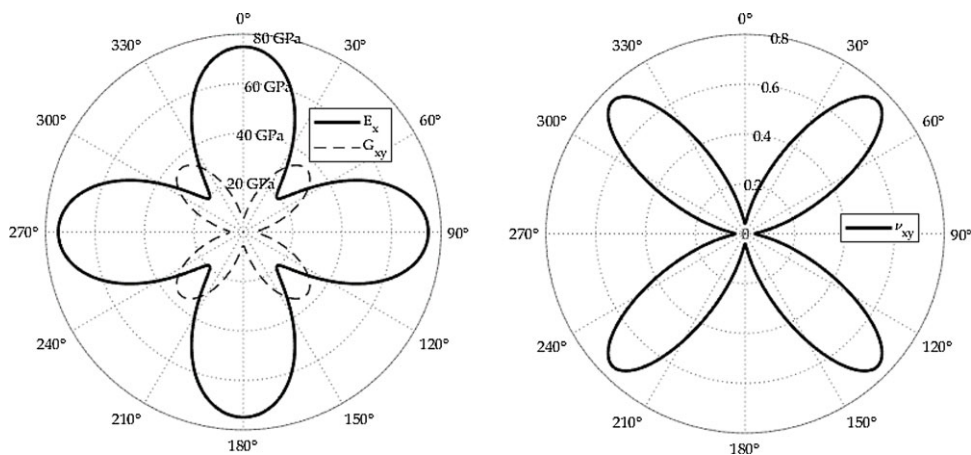$$E_x = A_{yy}^* - \frac{A_{xy}^{*2}}{A_{xx}^*} \tag{26.2}$$

$$v_{xy} = \frac{A_{xy}^*}{A_{yy}^*} \tag{26.3}$$

$$v_{yx} = \frac{A_{xy}^*}{A_{xx}^*} \tag{26.4}$$

$$G_{xy} = A_{ss}^* \tag{26.5}$$

Table 2. *Material properties of the composite for the given example*

Young's modulus	E_1	137.4	GPa
Young's modulus	E_2	11.71	GPa
Shear modulus	G_{12}	5.510	GPa
Poisson's ratio	ν_{12}	0.250	
Ply thickness	t_{ply}	0.200	mm

Figure 10. *Polar plots for modulus (left) and Poisson's ratio (right) dependent upon the material direction of orientation.*

Let us consider an orthotropic laminate with the following layup $[0, 0, 90, 90]_{2S}$, and material properties given in Table 2.

The resulting CLT analysis provides polar plots of the material properties as shown in Fig. 10.

The resulting phase velocities for both the symmetric and antisymmetric modes at 200 kHz are plotted in Fig. 11. As evident, the change in material properties has a marked effect upon the acoustic response of the panel and should be considered in any form of analysis.

5.3 Edge reflections

Edge reflections of Lamb waves has not been implemented but a proposed addition to the original numerical model is a raytracing method that would predict the path of the Lamb wave through a discrete number of angles, like that shown in Fig. 12. Boundary conditions can be implemented by considering whether the plate is fixed or free at an edge, resulting in an inverted or non-inverted reflection, respectively. Likewise, a relationship for reflected energy could be used to predict the amplitude of reflected waves as well as models for predicting mode conversion. Edge reflections are an important phenomenon, as the colocation of waves would result in constructive and destructive interference, affecting the ability to analyse and localise the emission.

Previous approaches including Monte Carlo simulations are computationally expensive, and hence, the use of ray tracing algorithms that can accurately and efficiently analyse the path of the wave from source to sink are desirable. Heinze et al. [53] developed a ray tracing algorithm for anisotropic composite materials based on Fermat's principle. Zhang et al. [54] proposed a novel version of the linear travel time interpolation method, which was also used to predict and visualise geometric defects in plates.
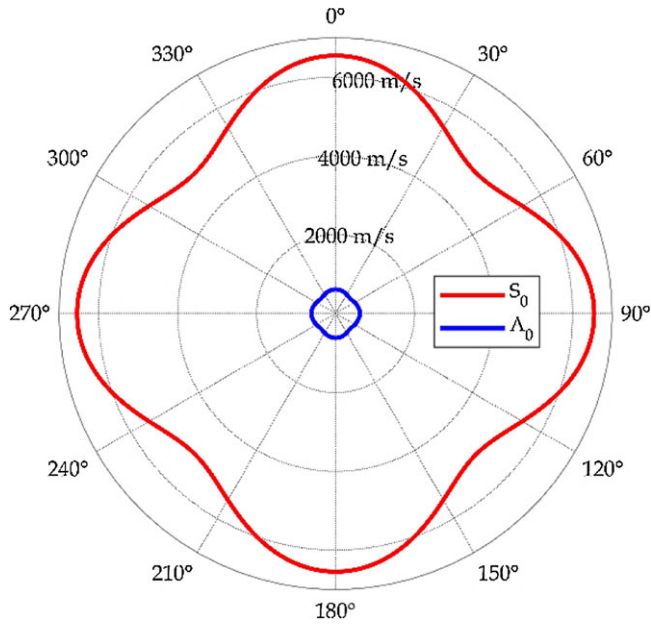
Figure 11. *Polar plot of the phase velocities of both Lamb wave modes.*
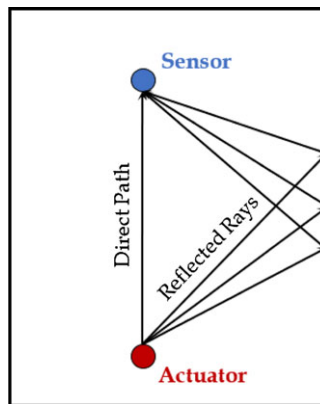

Figure 12. *The general principles of ray tracing edge reflections.*

Balvantín et al. [55] also developed a ray tracing method based on Fermat's principle by discretising the plate into a grid of constant material properties and applying Snell's law. A thickness reduction defect was experimentally and numerically studied, which showed the ability to reconstruct the tomography of a plate based upon the wave's time of flight.

6.0 Conclusion

Ultimately, this work has presented a novel first principles numerical model for predicting the behaviour of Lamb wave propagation in 2D plate structures. The model is easier to understand and implement compared to analytical solutions and faster than traditional numerical methods. Validation against WFR3 shows excellent correlation. The presented numerical model opens opportunities for improved NDT&E

and SHM of aerospace vehicles. The study also identifies potential avenues for future research and improvements to the code, including the modelling of high temperature effects, anisotropic materials and edge reflections. Overall, this research paper has contributed to the field of Lamb wave propagation modelling and provides valuable insights for researchers and engineers in the aerospace industry.

References

[1] Farley, M. 40 years of progress in NDT – History as a guide to the future, *AIP Conf. Proc.*, 2014, 1581, (1), pp 5–12, https://doi.org/10.1063/1.4864796

[2] Bond, L.J. Through the looking glass: The future for NDE?, *AIP Conf. Proc.*, 1581, 2014, (1), pp 21–35, https://doi.org/10.1063/1.4864798

[3] Grandt, F. Damage tolerant design and nondestructive inspection – keys to aircraft airworthiness, *Proc. Eng.*, 2011, vol. **17**, pp 236–246, https://doi.org/10.1016/j.proeng.2011.10.025

[4] Pollock, L., O'Byrne, S. and Wild, G. Quality assurance of uncured polymer matrix prepregs through the application of non-destructive methods, *NDT & E Int.*, 2023, **133**, p 102761.

[5] Staszewski, W., Boller, C. and Tomlinson, G.R. *Health Monitoring of Aerospace Structures: Smart Sensor Technologies and Signal Processing*. Wiley, 2004.

[6] Giurgiutiu, V., *Structural Health Monitoring with Piezoelectric Wafer Active Sensors*. Elsevier Science, 2014.

[7] Pollock, L. and Wild, G. Passive phased array acoustic emission localisation via recursive signal-averaged lamb waves with an applied warped frequency transformation, *arXiv preprint arXiv:2110.06457*, 2021, https://doi.org/10.48550/arXiv.2110.06457

[8] Rajagopal, P., Drozdz, M. and Lowe, M.J.S. Towards improved finite element modelling of the interaction of elastic waves with complex defect geometries, *AIP Conf. Proc.*, 2009, 1096, (1), pp 49–56, https://doi.org/10.1063/1.3114296

[9] Gresil, M., Shen, Y. and Giurgiutiu, V., Predictive modeling of ultrasonics SHM with PWAS transducers, Presented at the 8th International Workshop on Structural Health Monitoring, Stanford, CA, 13–15 Sep., 2011. [Online]. Available: http://www.me.sc.edu/research/lamss/pdf/conferences/C190_IWSHM_Predictive%20modeling%20of%20ultrasonics%20SHM%20with%20PWAS%20transducers_Matthieu%20Gresil.pdf

[10] Tuegel, E. The airframe digital twin: Some challenges to realization, Presented at the 53rd AIAA/ASME/ASCE/AHS/ASC Structures, Structural Dynamics and Materials Conference, Honolulu, HI, 23–26 Apr., 2012. [Online]. Available: https://doi.org/10.2514/6.2012-1812

[11] Glaessgen, E. and Stargel, D. The digital twin paradigm for future NASA and U.S. air force vehicles, Presented at the 53rd AIAA/ASME/ASCE/AHS/ASC Structures, Structural Dynamics and Materials Conference, Honolulu, HI, 23–26 Apr., 2012. [Online]. Available: https://doi.org/10.2514/6.2012-1818

[12] Li, L., Aslam, S., Wileman, A. and Perinpanayagam, S. Digital twin in aerospace industry: A gentle introduction, *IEEE Access*, 2022, **10**, pp 9543–9562, https://doi.org/10.1109/ACCESS.2021.3136458

[13] Yandouzi, M., Gaydos, S., Guo, D., Ghelichi, R. and Jodoin, B. Aircraft skin restoration and evaluation, *J. Therm. Spray Technol.*, 2014, **23**, (8), pp 1281–1290, https://doi.org/10.1007/s11666-014-0130-1

[14] Starke, E.A. and Staley, J.T. Application of modern aluminum alloys to aircraft, *Progr. Aerosp. Sci.*, 1996, **32**, (2), pp 131–172, https://doi.org/10.1016/0376-0421(95)00004-6

[15] Lamb, H. On waves in an elastic plate, *Proc. Roy. Soc. London. A, Contain. Papers Math. Phys. Char.*, 1917, 93, (648), pp 114–128.

[16] Rose, J.L. *Ultrasonic Waves in Solid Media*, Acoustical, Society of America, 2000.

[17] Worden, K. Rayleigh and lamb waves - Basic principles, *Strain*, 2001, **37**, (4), pp 167–172, https://doi.org/10.1111/j.1475-1305.2001.tb01254.x

[18] Giurgiutiu, V. *Structural Health Monitoring: With Piezoelectric Wafer Active Sensors*. Elsevier, 2007.

[19] Graff, K.F. Wave motion in elastic solids, Dover Publications.

[20] Bracewell, R.N. and Bracewell, R. *The Fourier Transform and Its Applications*. McGraw Hill, 2000.

[21] Sherafat, M.H., Quaegebeur, N., Hubert, P., Lessard, L. and Masson, P. Finite element modeling of Lamb wave propagation in composite stepped joints, *J. Reinfor. Plast. Compos.*, 2016, **35**, (10), pp 796–806, https://doi.org/10.1177/0731684416629763

[22] Sause, M.G., Hamstad, M.A. and Horn, S. Finite element modeling of lamb wave propagation in anisotropic hybrid materials, *Compos. B: Eng.*, **53**, 2013, pp 249–257, https://doi.org/10.1016/j.compositesb.2013.04.067

[23] Jingjing, H., Haode, H., Xuefei, G. and Jinsong, Y. A lamb wave quantification model for inclined cracks with experimental validation, *Chin. J. Aeronaut.*, 2020, https://doi.org/10.1016/j.cja.2020.02.010

[24] Ismail, N., Hafizi, Z., Nizwan, C. and Ali, S. "Simulation of Lamb wave interactions with defects in a thin plate, *J. Phys. Conf. Ser.*, 2019, **1262**, (1), p 012030, https://doi.org/10.1088/1742-6596/1262/1/012030

[25] Munian, R.K., Mahapatra, D.R. and Gopalakrishnan, S. Lamb wave interaction with composite delamination, *Compos. Struct.*, 2018, **206**, pp 484–498, https://doi.org/10.1016/j.compstruct.2018.08.072

[26] Marinushkin, P., Levitsky, A., Zograf, F. and Bakhtina, V. On the finite-element analysis of resonance MEMS structures based on acoustic lamb waves, *Informacije MIDEM*, 2020, **50**, (3), pp 179–188, https://doi.org/10.33180/infmidem2020.303

[27] Patera, A.T. A spectral element method for fluid dynamics: Laminar flow in a channel expansion, *J. Computat. Phys.*, 1984, **54**, (3), pp 468–488, https://doi.org/10.1016/0021-9991(84)90128-1

[28] Peng, H., Meng, G. and Li, F. Modeling of wave propagation in plate structures using three-dimensional spectral element method for damage detection, *J. Sound Vibr.*, 2009, **320**, (4–5), pp 942–954, https://doi.org/10.1016/j.jsv.2008.09.005.

[29] Sun, H., Zhang, A., Qing, X. and Wang, Y. Spectral element method for modeling Lamb wave interaction with open and closed crack, *J. Vibroeng.*, 2017, **19**, (7), pp 4965–4976, https://doi.org/10.21595/jve.2017.18284

[30] Ha, S. and Chang, F.-K. Optimizing a spectral element for modeling PZT-induced Lamb wave propagation in thin plates, *Smart Mater. Struct.*, 2009, **19**, (1), p 015015, https://doi.org/10.1088/0964-1726/19/1/015015

[31] Ahmad, Z. and Gabbert, U. Simulation of Lamb wave reflections at plate edges using the semi-analytical finite element method, *Ultrasonics*, 2012, **52**, (7), pp 815–820, https://doi.org/10.1016/j.ultras.2012.05.008

[32] Aalami, B. Waves in prismatic guides of arbitrary cross section, 1973, https://doi.org/10.1115/1.3423127

[33] Datta, S.K., Shah, A.H., Bratton, R. and Chakraborty, T. Wave propagation in laminated composite plates, *J. Acoust. Soc. Amer.*, 1988, **83**, (6), pp 2020–2026, https://doi.org/10.1121/1.396382

[34] Hladky-Hennion, A.-C. Finite element analysis of the propagation of acoustic waves in waveguides, *J. Sound Vibr.*, 1996, **194**, (2), pp 119–136, https://doi.org/10.1006/jsvi.1996.0349

[35] Gavrić, L. Computation of propagative waves in free rail using a finite element technique, *J. Sound Vibr.*, 1995, **185**, (3), pp 531–543, https://doi.org/10.1006/jsvi.1995.0398

[36] Hayashi, T., Song, W.-J. and Rose, J.L. Guided wave dispersion curves for a bar with an arbitrary cross-section, a rod and rail example, *Ultrasonics*, 2003, **41**, (3), pp 175–183, https://doi.org/10.1016/S0041-624X(03)00097-0

[37] Shorter, P. Wave propagation and damping in linear viscoelastic laminates, *The Journal of the Acoustical Society of America*, **2004**, **115**, (5), pp 1917–1925, https://doi.org/10.1121/1.1689342

[38] Ahmad, Z., Vivar-Perez, J.M. and Gabbert, U. Semi-analytical finite element method for modeling of lamb wave propagation, *CEAS Aeronaut. J.*, 2013, **4**, (1), pp 21–33, https://doi.org/10.1007/s13272-012-0056-6

[39] Peddeti, K. and Santhanam, S. Dispersion curves for Lamb wave propagation in prestressed plates using a semi-analytical finite element analysis, *J. Acoust. Soc. Amer.*, 2018, **143**(2), pp 829–840, https://doi.org/10.1121/1.5023335

[40] Hayashi, T. and Inoue, D. Calculation of leaky Lamb waves with a semi-analytical finite element method, *Ultrasonics*, 2014, **54**, (6), pp 1460–1469, https://doi.org/10.1016/j.ultras.2014.04.021

[41] Shen, Y. and Giurgiutiu, V. WaveFormRevealer: An analytical framework and predictive tool for the simulation of multi-modal guided wave propagation and interaction with damage, *Struct. Health Monitor.*, 2014, **13**, (5), pp 491–511.

[42] Haugwitz, C., Hinrichs, J., Rutsch, M., Allevato, G., Dörsam, J.H. and Kupnik, M. Lamb wave reflection and transmission in bent steel sheets at low frequency, In 2022 *IEEE International Ultrasonics Symposium (IUS)*, 2022: IEEE, pp 1–4.

[43] Cirtautas, D., Samaitis, V., Mažeika, L., Raišutis, R. and Žukauskas, E. Selection of higher order lamb wave mode for assessment of pipeline corrosion, *Metals*, 2022, **12**, (3), p 503.

[44] Yu, F.-m., Okabe, Y., Wu, Q. and Shigeta, N. A novel method of identifying damage types in carbon fiber-reinforced plastic cross-ply laminates based on acoustic emission detection using a fiber-optic sensor, *Compos. Sci. Technol.*, 2016, **135**, pp 116–122, https://doi.org/10.1016/j.compscitech.2016.09.017

[45] Giurgiutiu, V. Tuned Lamb wave excitation and detection with piezoelectric wafer active sensors for structural health monitoring, *J. Intell. Mater. Syst. Struct.*, 2005, **16**, (4), pp 291–305, https://doi.org/10.1177/1045389X05050106

[46] Pollock, L., Wild, G., Abdelwahab, A.K. and Murray, J. The Need for Aerospace Structural Health Monitoring: A review of aircraft fatigue accidents, *Int. J. Prognost. Health Manag.*, 2021, **12**, (3), https://doi.org/10.36001/ijphm.2021.v12i3.2368

[47] Pollock, L. and Wild, G., "An initial review of hypersonic vehicle accidents," in *AIAC* 2021*: 19th Australian International Aerospace Congress: 19th Australian International Aerospace Congress*, 2021: Engineers Australia, pp 111–116, https://doi.org/10.48550/arXiv.2110.06438

[48] Ashby, M.F., Shercliff, H. and Cebon, D. *Materials: Engineering, Science, Processing and Design*. Butterworth-Heinemann, 2018.

[49] Augereau, F., Laux, D., Allais, L., Mottot, M. and Caes, C. Ultrasonic measurement of anisotropy and temperature dependence of elastic parameters by a dry coupling method applied to a 6061-T6 alloy, *Ultrasonics*, 2007, **46**, (1), pp 34–41, https://doi.org/10.1016/j.ultras.2006.10.002

[50] Pollock, L. and Wild, G. Spectral domain analysis of acousto-ultrasonic tone burst lamb wave emissions in uncured pre-preg carbon fiber composites, In *ASCEND* 2021, 2021, p 4233.

[51] Wierach, P. *Lamb-Wave based Structural Health Monitoring in Polymer Composites*. Springer, 2017.

[52] Baker, A.A. *Composite Materials for Aircraft Structures*. AIAA, 2004.

[53] Heinze, C., Sinapius, M. and Wierach, P. Lamb wave propagation in complex geometries-model reduction with approximated stiffeners, In *EWSHM-7th European Workshop on Structural Health Monitoring*, 2014.

[54] Zhang, H., Sun, X., Qi, X. and Liu, Q. A modified LTI ray tracing algorithm in Lamb wave tomography, In 2008 *International Conference on Audio, Language and Image Processing*, 2008, IEEE, pp 1059–1062, https://doi.org/10.1109/ICALIP.2008.4590287

[55] Balvantín, A., Baltazar, A. and Rodriguez, P. Characterization of laser generated Lamb wave modes after interaction with a thickness reduction discontinuity using ray tracing theory, *Exp. Mech.*, 2014, **54**, 743–752, https://doi.org/10.1007/s11340-013-9846-y